Effect of Y, La, and Yb simultaneous doping on the thermal conductivity and thermoelectric performances of $CaMnO_3$ ceramics

Maria A. Madre[1], Hippolyte Amaveda[1], Oscar J. Dura[2], Denis Pelloquin[3], Mario Mora[1], Miguel A. Torres[1], Sylvain Marinel[2], Andres Sotelo[1,*]

[1]Instituto de Nanociencia y Materiales de Aragón (CSIC-Universidad de Zaragoza), Mª de Luna, 3. 50018-Zaragoza, Spain.

[2]Departamento de Física Aplicada (Universidad de Castilla-La Mancha), 13071-Ciudad Real, Spain.

[3]Normandie Univ, ENSICAEN, UNICAEN, CNRS, CRISMAT, 14000 Caen, France.

Abstract

Triple doping of $CaMnO_3$ in different stoichiometric proportions has been studied in bulk sintered materials. They were prepared through the classical ceramic route using planetary milling to decrease the precursors particle sizes. It has been found that particle sizes decrease with the amount of dopant, both in the precursors and in the sintered bodies. XRD patterns showed that all samples were nearly single phase, with small amounts of $CaMn_2O_4$ phase. SEM and TEM observations revealed a homogeneous distribution of dopants in the $CaMnO_3$ phase, while EDX showed a composition close to the nominal one. However, HREM imaging has shown some dark regions in the crystallites, with different Ca(Y,La,Yb)/Mn ratios found through STEM image-chemical mapping, which points out to the coexistence of $CaMnO_3$ and $CaMn_2O_4$–type domains in the crystallites. Electrical resistivity, absolute Seebeck coefficient and thermal conductivity have been drastically decreased with doping. The highest PF

values at 800 ºC have been achieved in 0.02(Y,La,Yb) doped samples (~ 0.37 mW/K^2m), which is among the best reported values in literature. On the other hand, lattice thermal conductivity is dramatically decreased with doping due to the phonon scattering produced by the dopants, the decrease in the grain sizes, and the strains present inside the crystallites, reaching the minimum values at 800 ºC in 0.03(Y,La,Yb) doped samples (~ 0.8 W/K m). Consequently, ZT reaches the maximum values (~ 0.29) in 0.03(Y,La,Yb) doped samples due to their very low thermal conductivity, being higher than the best ZT reported values in the literature.

Keywords: Ceramic material, Electroceramics, Oxides, Electrical properties, Thermal conductivity, Thermoelectrics

* Corresponding author: A. Sotelo

E-mail: asotelo@unizar.es

Address: Dept. Ciencia de Materiales; C/Mª de Luna, 3; 50018-Zaragoza; Spain

Tel: +34 976762617

Fax: +34 976761957

1. Introduction

In the present world situation, with fossil fuels and energy costs increasing day-by-day, the relatively low energy conversion efficiency of classical systems is an important drawback. Consequently, the search for new renewable energy generation systems, as well as the increase of efficiency of classical systems should be a priority for all countries. In this situation, thermoelectric (TE) technology can be regarded as one of the most promising methods to produce useful energy from wasted and/or renewable heat sources [1]. Furthermore, this technology can play an important role in fighting against global warming by decreasing CO_2 emissions and reducing the fossil fuel consumption. For this purpose, it is necessary to have TE materials with high performances, determined through the dimensionless figure of merit, ZT (= $TS^2/\rho\kappa$; T absolute temperature, S Seebeck coefficient, ρ electrical resistivity, and κ thermal conductivity) [2].

High performance state-of-the-art materials are mainly semiconducting and intermetallic compounds, which are used to fabricate commercial TE modules. On the other hand, these materials are composed of scarce, expensive, heavy and/or toxic elements [3-7]. Moreover, they can melt, evaporate or oxidize at high temperatures under air, drastically limiting their range of applications. However, the discovery of relatively high thermoelectric performances in Na_xCoO_2 [8], provided a solution for some of those problems. This material is composed of non-toxic, more abundant, and cheaper elements than the classical ones [6,7]. Furthermore, it can operate at high temperatures for a long time under air without degradation. These characteristics led to an intense research on these ceramic materials, allowing identifying other promising CoO-

based compounds [9,10], which showed p-type conduction. Moreover, these works also allowed identifying other ceramic compounds with n-type conduction [11,12]. However, their thermoelectric performances should still be increased for practical and massive applications [13].

Among n-type compounds, one of the most promising for practical applications is $CaMnO_3$ due to its high thermal stability, and the relatively high abundance of Ca and Mn in the earth crust. However, they are typically electronically doped to increase their electrical conductivity to achieve optimal thermoelectric properties [14-16]. Besides, it is also possible to achieve high electrical conductivity through alternative synthesis methods [17-19], and/or processing techniques [20-22], which can affect the initial particle sizes and/or the final sample density. On the other hand, it is well known that increasing electrical conductivity leads to the increase in thermal conductivity, which can also be affected by the substitutional defects and nanograins formation due to phonon scattering [23]. Consequently, the objective of this work is enhancing the thermoelectric performances of $CaMnO_3$ by increasing its electrical conductivity by Y, La, and Yb triple doping in the Ca-site, and planetary milling to decrease initial particle size. The fact of selecting these elements as dopants is due to their different atomic weight, which could scatter different wavelength phonons, increasing their effect on the lattice thermal conductivity. The thermoelectric properties of the final sintered materials will be evaluated and related to their structural and microstructural features.

2. Experimental

The initial $Ca_{1-3x}Y_xLa_xYb_xMnO_3$ mixtures, with x= 0, 0.01, 0.02, and 0.03 used in this work were prepared from $CaCO_3$ (≥ 99%, Aldrich), Y_2O_3 (99.99%, Aldrich), La_2O_3 (≥ 99.9%, Aldrich),Yb_2O_3 (99.9%, Aldrich), and Mn_2O_3 (99%, Aldrich) commercial precursors. The powders were weighed in appropriate proportions, thoroughly mixed and milled in a planetary mill in water, using ZrO_2 balls as milling media, at 400 rpm for 4 h. The homogeneous mixture was dried in an oven at 60 ºC, and the dry powder was calcined in two steps, at 950, and 1050 ºC for 12 h, being intermediately manual milled. These pre-reacted materials were subsequently subjected to planetary milling, in the same conditions previously described and dried. The resulting powder was finally cold uniaxially pressed at about 400 MPa in form of pellets (~ 3 x 3 x 14 mm^3) and sintered at 1300 ºC for 12 h with a final furnace cooling.

Powder particle size was determined in samples before uniaxial pressing in a Zetasizer nano (Malvern Panalytical). Phase identification in the sintered materials has been performed from powder X-ray diffraction (XRD) data collected with a Rigaku Ru300 X-ray powder diffractometer working with copper anticathode (λ=1.5406Å) with 2θ ranging between 5 to 60 º. Moreover, these data have been used to perform Rietveld analyses with Fullprof Suite software distributed by Roisnel et al. [24]. Microstructural observations were performed on the samples surfaces in a field emission scanning electron microscope (FESEM Zeiss Merlin), fitted with an energy-dispersive X-ray spectrometer (EDX) used to determine the elemental composition of grains. Moreover, grain size has been evaluated using the line intercept method [25] in several micrographs for each composition. A transmission electronic microscopy study has been performed on the $Ca_{1-3x}Y_xLa_xYb_xMnO_3$ series to probe the doping

homogeneity, the purity and quality of the stacking at the crystalline scale. Firstly, the samples were ground in a mortar with a butanol solution. A fine droplet of this mixture was picked up and deposited on a nickel grid. The TEM observations were carried out with a F200 JEOL cold FEG microscope with a resolution point of 2.3Å equipped with a Centurio EDX analyser and a digital RIO16 camera. The raw data were treated and formatted with the Digital Micrograph (GATAN) and Analysis Station (JEOL) softwares. For each sample, the images were recorded with different magnifications in order to judge the whole shape and the distribution of the cristallites and their average size. The higher magnification TEM images and their corresponding Fourier Form Transformation (FFT) were used to identify the zone axes and the potential defects illustrating these (Y,La,Yb)-doped $CaMnO_3$ manganites. Moreover, the most doped sample, $Ca_{0.91}Y_{0.03}La_{0.03}Yb_{0.03}MnO_3$, was also analysed by STEM (Scanning transmission electron microscopy) techniques. Especially, the chemical distribution was probed owing to the coupled atomic STEM imaging-EDX mapping experiments to reveal the local cation distribution at the level of strains.

Density of samples has been determined through the well-known Archimedes' method in several samples for each composition. Electrical resistivity and Seebeck coefficient were simultaneously determined for all samples, in steady state mode, by the standard dc four-probe technique in a LSR-3 apparatus (Linseis GmbH) between 50 and 800 ºC under He atmosphere. With the electrical resistivity and Seebeck coefficient values, PF (= $S2/\rho$) has been calculated to determine the electrical performances.

The thermal diffusivity (α) has been determined in all samples in a laser-flash system (Linseis LFA 1000). The thermal conductivity (κ) was obtained using the formula:

$$\kappa = \alpha C_p \rho$$

where C_p is the specific heat, calculated through the well-known Dulong-Petit law, and ρ is the sample density. Finally, using PF and thermal conductivity values, ZT has been calculated to evaluate the TE performances of these materials.

In order to simplify the samples nomenclature, they will be named as x(Y,La,Yb), being x the value in $Ca_{1-3x}Y_xLa_xYb_xMnO_3$ formula (x = 0.0, 0.01, 0.02, and 0.03).

3. Results and discussion

The powder microstructure, before the cold uniaxial pressing procedure, has been observed through SEM microscopy. In Fig. 1, representative micrographs of the different powders are displayed. As it can be seen, all samples present very similar grain aspect. Moreover, they are formed by a mixture of relatively large and small grains, and the proportion of small ones seems to be enhanced when the dopant content is increased. This fact points out to the capability of the rare earth dopants to inhibit grain growth. In order to confirm this result, particle size measurements have been performed through Z-potential technique, and the results are shown in Table 1. These results clearly show that the increase of the dopant amount leads to an important decrease of the starting particle sizes of precursors.

After sintering, the materials were studied through powder XRD, and the results are illustrated in Fig. 2, for 2θ ranging from 20 to 50 º. As it can be seen in the graph, all samples present the same diffraction data set that can be identified in a Pnma space group, in agreement with the reported results [26]. This result clearly shows that the $CaMnO_3$ samples are almost single phase provided by the high reactivity of precursor powders due to their small mean sizes. In order to judge the actual doping and its impact on the cell parameters evolution, a Rietveld analysis has been carried out for each composition considering the Pnma settings reported for the pristine $CaMnO_3$ [26]. This work is summarized in Table 2, where it can be observed that the parameters gradually increase with the x value, in agreement with the ionic radii of dopants (La^{3+} = 1.17 Å > Y^{3+} = 1.04 Å > Yb^{3+} = 1.008 Å) compared to Ca^{2+} (1.00 Å). More instructive, these analyses have pointed out some unindexed small peaks (red arrows) as illustrated by the enlarged part of difference spectrum shown in Fig. 2b. Some complementary experiments have been performed by electron microscopy, especially from EDX experiments at the crystallite scale, to identify these extra peaks. The spectroscopic approach coupled to the electron diffraction study has allowed confirming the Pnma setting related to the $CaMnO_3$-type structure and that the doping levels are close to the nominal ones. For instance, the average $(Ca_{0.83}Y_{0.04}La_{0.04}Yb_{0.02})_{0.94}MnO_3$ composition has been obtained from 10 analyzed crystallites for the nominal $Ca_{1-3x}Y_xLa_xYb_xMnO_3$ composition. Except to the lower Yb content compared to La and Y species and a slight Ca deficit, the chemical mappings are rather homogeneous, as illustrated in Fig. 3a, suggesting a regular stacking mode. On the other hand, the Ca deficit can suggest the existence of local stacking faults or the presence of Mn rich

inclusions. The first hypothesis has been invalidated through atomic TEM observations, where no evident defects have been identified, as it can be observed in Fig. 3b. Only some darker regions can be observed in the HREM imaging suggesting the coexistence of extended domains. Complementary coupled atomic STEM image-chemical mapping performed on such zones have not highlighted some local changes of dopants concentration (Fig. 3c). However, it revealed that the ratio (Ca,Y,La,Yb)/Mn varies from 0.85 to 0.94 from side to side of this peculiar contrast, as illustrated by the elemental line profiles shown in Fig. 3d. Such an evolution suggests the presence of a Mn richer domain that could be related to the $CaMn_2O_4$ marokite-type phase [27]. This hypothesis is validated by the Rietveld analysis introducing the Pbcm secondary phase related to the marokite structure. The reliability R_{bragg} factors are noticely decreased and all extra small unknown peaks are indexed (Fig. 2b). According to the final Rietveld refinements, the amount of secondary phase ranges from 1.35 to 3.47% in volume, as listed in Table 2. The coexistence of both structures, namely perovskite and $CaMn_2O_4$-type structures would lead to internal stresses in the crystal matrix. Consequently, when re-evaluating the results of EDX experiments leading to the mean $(Ca_{0.83}Y_{0.04}La_{0.04}Yb_{0.02})_{0.94}MnO_3$ composition, the coexistence of $(Ca,Y,La,Yb)Mn_2O_4$ extended domains inside $(Ca,Y,La,Yb)MnO_3$ as main matrix, could be advanced.

Representative SEM micrographs of the samples surfaces, taken using backscattered electrons, are displayed in Fig. 4. These images illustrate the very high density achieved after sintering. In order to confirm these observations, Archimedes' method has been used to determine the samples density. The obtained values, together with their standard error, are displayed in

Table 3. These data clearly show that the absolute density increases with the amount of dopants, and it is ranging between 89 and 94 % of the theoretical one of $CaMnO_3$ (4.705 g/cm^3) [28], which are very high when compared to classically sintered materials (~ 75 %) [29].

Other important features that can be seen in these images is that grain sizes decrease when the amount of dopants is increased, as it is displayed in Fig. 4. These images illustrate the drastic grain size reduction by comparing the undoped samples (Fig. 4a) to the 0.03-doped ones (Fig. 4b). The mean grain sizes, together with their standard error, determined in several micrographs by the line intercept method are shown in Table 3. These data clearly point out to the effect of dopants on the grain size, which are acting as grain growth inhibitors. On the other hand, EDX analysis performed on these samples (not shown) has only identified the $Ca_{1-3x}Y_xLa_xYb_xMnO_3$ phase, with a slight deficiency in Ca, in agreement with the TEM-EDX results.

Fig. 5 shows the temperature dependence of the electrical resistivity, as a function of the samples composition. At first sight, it is easy to observe that the undoped sample possesses a marked semiconducting-like character ($d\rho/dT < 0$), in agreement with previously reported data in this system [30,31]. On the other hand, doping leads to a drastic reduction of electrical resistivity, due to the slight enhancement of density, and the increase of charge carrier concentration by the substitution of Ca^{+2} by Y^{3+}, La^{3+}, and Yb^{3+}. Moreover, there are also differences between the doped samples, as it is illustrated in the insert, where it can be observed that electrical resistivity is decreased with the dopants content in the whole measured temperature range, due to the increase of density and charge carrier concentration. However, the differences between doped samples

are decreased when the doping content is increased due to the grain size reduction. Consequently, the number of grain boundaries, usually more resistive than the intragrain regions, are increased and tend to increase electrical resistivity, counter balancing the effect of electron doping. The minimum values at 800 ºC have been reached in 0.03(Y,La,Yb)-substituted samples (5.8 mΩ cm), which is similar to the reported in Pr and Sr co-doped $CaMnO_3$ prepared by sol-gel method (~ 5.5 mΩ cm) [32]. Moreover, it is much lower than the best reported in the literature for laser grown samples (9 mΩ cm) [21], or in electronic doped materials (10-12 mΩ cm) [16,33,34].

The evolution of Seebeck coefficient with temperature, as a function of the dopants content is presented in Fig. 6. All samples exhibit negative Seebeck values in the whole studied temperature range, confirming a dominating electronic conduction mechanism. As it can be observed in the graph, absolute S values are decreased when the amount of dopants is increased, clearly reflecting the effect of these elements on the charge carrier concentration, as already mentioned in the electrical resistivity discussion. Moreover, rare earth doping drastically changes the |S| behaviour with temperature. In the undoped samples |S| values are decreasing when the temperature is raised, while it increases with temperature in all doped samples. The behaviour of these doped materials can be associated to that of a metal or degenerated semiconductor when the variation of carrier concentration, effective mass, and Fermi level with temperature are negligible [35]. Furthermore, it can be deduced that the undoped samples increase their charge carrier concentration with temperature, being reflected in the drastic decrease of electrical resistivity, as well as the rise of |S|, with temperature. The highest |S| value at 800 ºC in 0.03(Y,La,Yb)-doped

samples (140 μV/K) is similar to those reported in the literature for similarly doped materials (120-160 μV/K) [16,32-34].

The electrical performances of these samples have been determined through the PF values obtained from the electrical resistivity and Seebeck coefficient data. These data are presented in Fig. 7 as a function of temperature and dopants content. As it can be observed in the graph, PF increases with the dopants content up to 0.02(Y,La,Yb), decreasing for higher amount, in the whole measured temperature range. Moreover, it is regularly increased when the temperature is raised, mainly reflecting the increase of absolute Seebeck coefficient with temperature. Consequently, the highest value has been obtained at 800 ºC for the 0.02(Y,La,Yb) samples (~ 0.37 mW/K^2m), which is much higher than the reported in similarly doped materials (0.17-0.25 mW/K^2m) [16,33,34], and in the order of best reported in co-doped $CaMnO_3$ (0.095-0.38 mW/K^2m) [32,36-38].

In Fig. 8, the total thermal conductivity is presented for all samples. As it can be observed, the thermal conductivity is drastically decreased by doping, and further decreased with the dopants content. The minimum values at 800 ºC are observed in the 003(Y,La,Yb) doped samples (1.24 W/K m), which is nearly 3 times lower than the measured in undoped ones (3.33 W/K m). Moreover, it is much lower than the reported in electronically doped $CaMnO_3$ materials (1.40-3.60 W/K m) [11,14,15,32,39,40]. The large decrease of thermal conductivity with doping is associated with the introduction of much higher atomic weight cations than Ca^{2+} which can effectively increase phonon scattering. Furthermore, another important effect induced by doping is the decrease of the mean grain sizes, which can further decrease this phonon scattering. As it is

well known, total thermal conductivity can be divided into two contributions $\kappa = \kappa_{ph} + \kappa_e$, where κ_{ph}, and κ_e are the phononic (lattice), and electronic contribution, respectively. These contributions are shown separately in Fig. 9. As it can be observed in the graph, electronic contribution is increased with the amount of dopant and temperature, in agreement with the observed behaviour of electrical resistivity. On the other hand, the lattice contribution to thermal conductivity is drastically reduced with doping. This effect is associated to phonon scattering at different frequencies produced by the introduction of dopants with different atomic weight. Additionally, it has to be also considered the effect, on the lattice thermal conductivity, the presence of previously mentioned stresses on the crystal structure found through the TEM image (see Fig. 3).

This evolution of lattice thermal conductivity has been analysed in terms of the Callaway's model [41] to validate it by using the parameters obtained in this work. Therefore, the model includes the boundary scattering, the Umklapp phonon-phonon scattering, and the point defects scattering [42]. The results of the analysis are shown in Fig. 10, where it can be observed that they perfectly reproduce the thermal evolution of κ_{ph} for all samples. From these fittings, the point defects and the phonon-phonon interactions have been compared, and the results are displayed in Table 4. As it can be observed in these data, the effect due to the point defects are increased when the amount of dopant is raised, whereas a similar trend can be seen in the phonon-phonon interactions, even if the result obtained for the 0.01(Y,La,Yb) sample is lower than the expected.

Finally, using PF and κ data, ZT has been calculated for all samples. The obtained graph is presented in Fig. 11 as a function of temperature and dopants

content. As it can be easily seen in the plot, the highest ZT values have been obtained for the 0.03(Y,La,Yb)-doped sample (~ 0.29 at 800 ºC), mainly due to its very low thermal conductivity. These values are more than three times higher than the obtained in undoped samples in this work (~ 0.09 at 800 ºC). Moreover, it is higher than the best reported for doped $CaMnO_3$ (0.08-0.25 at similar temperatures) [11,14,39,40,43-46].

The high ZT values obtained in $CaMnO_3$ samples using Y, La, and Yb co-doping, combined with the decrease of the starting particle sizes make these sintered materials very promising candidates to be used in high temperature thermoelectric devices for practical applications in waste heat harvesting.

4. Conclusions

In this work, the effect of a triple substitution (Y, La, and Yb) in the A-site of $CaMnO_3$ has been studied. Samples were prepared through the solid-state reaction using planetary milled precursors to reduce starting particle sizes. It has been found that particle sizes are decreased when the dopant content is increased, both in the milled and sintered materials. XRD has shown that all samples are nearly single phase, with small amounts of $CaMn_2O_4$ secondary phase found through Rietveld analysis. Moreover, it has been found that cell parameters are increased with the amount of dopants due to their larger ionic radii, when compared to that of Ca. SEM and TEM observations showed that dopants are well distributed in the $CaMnO_3$ crystal structure, and that their overall composition is very close to the nominal one, with no evidence of secondary phase. However, HREM imaging has shown some dark regions in the crystallites. STEM image-chemical mapping performed in these zones has

found that Ca(Y,La,Yb)/Mn ratio varies across the dark area, pointing out to the coexistence of $CaMnO_3$ and $CaMn_2O_4$ structures in the crystallites. Electrical resistivity is drastically decreased with doping, as well as the absolute Seebeck coefficient due to the increase of charge carrier concentration. The highest PF at 800 ºC has been obtained in 0.02(Y,La,Yb) doped samples (~0.37 mW/K^2m), which is in the order of the best reported in the literature. Lattice and total thermal conductivity have been dramatically reduced by doping, reaching the minimum values at 800 ºC in 003(Y,La,Yb) doped samples (0.80, and 1.24 W/K m, respectively), which are the lowest value reported in the literature for bulk sintered materials, in the best of our knowledge. Moreover, the thermal evolution of lattice thermal conductivity is in agreement with the Debye/Callaway model, using the parameters obtained in this work. Finally, the highest ZT values have been reached in the 003(Y,La,Yb) doped samples (~ 0.29 at 800 ºC) provided by their very low electrical resistivity and thermal conductivity. Furthermore, this value is the highest obtained in bulk $CaMnO_3$ ceramics in the best of our knowledge.

Acknowledgements

Authors would like to acknowledge the use of Servicio General de Apoyo a la Investigación-SAI, Universidad de Zaragoza. Xavier Larose (CRISMAT Laboratoire-Caen) is also acknowledged by his technical support about TEM investigations.

Funding: This work was supported by the Gobierno de Aragón (Grupo de Investigacion Consolidado T54_20R)

References

[1] M. H. Elsheikh, D. A. Shnawah, M. F. M. Sabri, S. B. M. Said, M. H. Hassan, M. B. A. Bashir, M. Mohamad, A review on thermoelectric renewable energy: Principle parameters that affect their performance, Renew. Sust. Energy Rev. 30 (2014) 337-355.

[2] D. M. Rowe in: D. M. Rowe (ed.), Thermoelectrics Handbook: Macro to Nano, CRC Press, Boca Raton, FL., 2006.

[3] H. Wang, J. Hwang, M. L. Snedaker, I.-H. Kim, C. Kang, J. Kim, G. D. Stucky, J. Bowers, W. Kim, High thermoelectric performance of a heterogeneous PbTe nanocomposite, Chem. Mater. 27 (2015) 944-949.

[4] A. C. Sklad, M. W. Gaultois, A. P. Grosvenor, Examination of $CeFe_4Sb_{12}$ upon exposure to air: is this material appropriate for use in terrestrial, high-temperature thermoelectric devices?, J. Alloy. Compd. 505 (2010) 6-9.

[5] A. A. Yaroshevsky, Abundances of chemical elements in the earth's crust, Geochem. Int. 44 (2006) 48-55.

[6] J. He, Y. Liu, R. Funahashi, Oxide thermoelectrics: The challenges, progress, and outlook, J. Mater. Res. 26 (2011) 1762-1772.

[7] S. LeBlanc, Thermoelectric generators: Linking material properties and systems engineering for waste heat recovery applications, Sust. Mater. Technol. 1-2 (2014) 26-35.

[8] I. Terasaki, Y. Sasago, K. Uchinokura, Large thermoelectric power in $NaCo_2O_4$ single crystals, Phys. Rev. B 56 (1997) 12685-12687.

[9] A. C. Masset, C. Michel, A. Maignan, M. Hervieu, O. Toulemonde, F. Studer, B. Raveau, J. Hejtmanek, Misfit-layered cobaltite with an anisotropic giant magnetoresistance: $Ca_3Co_4O_9$. Phys. Rev. B 62 (2000) 166-175.

[10] R. Funahashi, I. Matsubara, H. Ikuta, T. Takeuchi, U. Mizutani, S. Sodeoka, An Oxide Single Crystal with High Thermoelectric Performance in Air, Jpn. J. Appl. Phys. 39 (2000) L1127-L1129.

[11] Y.-H. Zhu, W.-B. Su, J. Liu, Y.-C. Zhou, J. Li, X. Zhang, Y. Du, C.-L. Wang, Effects of Dy and Yb co-doping on thermoelectric properties of $CaMnO_3$ ceramics, Ceram. Int. 41 (2015) 1535-1539.

[12] J. Liu, C. L. Wang, Y. Li, W. B. Su, Y. H. Zhu, J. C. Li, L. M. Mei, Influence of rare earth doping on thermoelectric properties of $SrTiO_3$ ceramics, J. Appl. Phys. 114 (2013) 223714.

[13] K. Koumoto, I. Terasaki, R. Funahashi, Complex Oxide Materials for Potential Thermoelectric Applications, MRS Bull. 31 (2006) 206-210.

[14] M. Ohtaki, H. Koga, T. Tokunaga, K. Eguchi, H. Arai, Electrical Transport properties and High-Temperature thermoelectric Performances of $(Ca_{0.9}M_{0.1})MnO_3$ (M= Y, La, Ce, Sm, In, Sn, Sb, Pb, Bi), J. Solid State Chem. 120 (1995) 105-111.

[15] T. Wang, P. F. Nan, H. C. Wang, W. B. Su, A. Sotelo, J. Z. Zhai, X. Wang, Y. Z. Ran, T. T. Chen, C. L. Wang, Right Heterogeneous Microstructure for Achieving Excellent Thermoelectric Performance in $Ca_{0.9}R_{0.1}MnO_{3-\delta}$ (R = Dy, Yb) Ceramics, Inorg. Chem. 57 (2018) 9133-9141.

[16] D. Flahaut, T. Mihara, R. Funahashi, N. Nabeshima, K. Lee, H. Ohta, K. Koumoto, Thermoelectrical properties of A-site substituted $Ca_{1-x}Re_xMnO_3$ system. J. Appl. Phys. 100 (2006) 084911.

[17] H. Taguchi, M. Io, M. Yoshinaka, K. Hirota, O. Yamaguchi, Low-temperature synthesis of perovskite-type $(Nd_{1-x}Ca_x)MnO_3$ (0.0 <= x <= 0.5) via polymerized complex route, Solid State Ionics 172 (2004) 611-615.

[18] L. Y. Qi, S. Hao, Y. J. Li, Microstructure and electrical properties of $Ca_{1-x}Er_xMnO_{3-\delta}$ powders prepared by hydrothermal technique, Res. Chem. Intermed. 43 (2017) 153-162.

[19] A. Sotelo, M. A. Madre, M. A. Torres, J. C. Diez, Effect of synthesis process on the densification, microstructure, and electrical properties of $Ca_{0.9}Yb_{0.1}MnO_3$ ceramics, Int. J. Appl. Ceram. Technol. 14 (2017) 1190-1196.

[20] V. H. Crespi, L. Lu, Y. X. Jia, K. Khazeni, A. Zettl, M. L. Cohen, Thermopower of single-crystal $Nd_{1-x}(Sr,Pb)_xMnO_{3-\delta}$, Phys. Rev. B 53 (1996) 14303-14308.

[21] N. M. Ferreira, N. R. Neves, M. C. Ferro, M. A. Torres, M. A. Madre, F. M. Costa, A. Sotelo, A. V. Kovalevsky, Growth rate effects on the thermoelectric performance of $CaMnO_3$-based ceramics, J. Eur. Ceram. Soc. 39 (2019) 4184-4188.

[22] S. J. Han, Y. K. Chen, S. Sampath, Role of process conditions on the microstructure, stoichiometry and functional performance of atmospheric plasma sprayed $La(Sr)MnO_3$ coatings, J. Power Sources 259 (2014) 245-254.

[23] G. H. Zhu, H. Lee, Y. C. Lan, X. W. Wang, G. Joshi, D. Z. Wang, J. Yang, D. Vashaee, H. Guilbert, A. Pillitteri, M. S. Dresselhaus, G. Chen, Z. F. Ren, Increased Phonon Scattering by Nanograins and Point Defects in Nanostructured Silicon with a Low Concentration of Germanium, Phys. Rev. Lett. 102 (2009) 196803.

[24] T. Roisnel, J. Rodriguez-Carvajal, WinPLOTR, a graphic tool for power diffraction, https://cdifx.univ-rennes1.fr/winplotr/winplotr.htm. 20th, January, 2023.

[25] E. Heyn, Short reports from the metallurgical and metallographical laboratory of the Royal Mechanical and Technical Testing Institute of Charlottenburg, The Metallographist 5 (1903) 39-64.

[26] K. R. Poeppelmeier, M. E. Leonowicz, J. C. Scanlon, J. M. Longo, W. B. Yelon, Structure determination of $CaMnO_3$ and $CaMnO_{2.5}$ by X-ray and neutron methods, J. Solid State Chem. 45 (1982) 71-79.

[27] J. Zagorac, A. Zarubica, A. Radosavljevic-Mihajlovic, D. Zagorac, B. Matovic, Structural study of nanosized yttrium-doped $CaMnO_3$ perovskites, Bull. Mater. Sci. 37 (2014) 407-416.

[28] R. Lohnert, M. Stelter, J. Topfer, Evaluation of soft chemistry methods to synthesize Gd-doped $CaMnO_{3-\delta}$ with improved thermoelectric properties, Mater. Sci. Eng. B 223 (2017) 185-193.

[29] A. Sotelo, M. A. Torres, M. A. Madre, J. C. Diez, Role of Ag on the properties of $Ca_{0.9}Yb_{0.1}MnO_3$ sintered ceramics, Materials 11 (2018) 2503.

[30] N. Kanas, B. A. D. Williamson, F. Steinbach, R. Hinterding, M.-A. Einarsrud, S. M. Selbach, A. Feldhoff, K. Wiik, Tuning the Thermoelectric Performance of $CaMnO_3$-Based Ceramics by Controlled Exsolution and Microstructuring, ACS Appl. Energy Mater. 5 (2022) 12396-12407.

[31] A. Vijay, S. C. Prasanth, R. Jose, P. Vineetha, K. V. Saravanan, A Study on the Effects of La/Sm Codoping on the Structural and High Temperature Thermoelectric Properties of n-Type $CaMnO_{3-\delta}$ Perovskite, Cryst. Res. Technol. 57 (2022) 2200041.

[32] K. K. Liu, Z. Y. Liu, F. P. Zhang, J. X. Zhang, X. Y. Yang, J. W. Zhang, J. L. Shi, G. Ren, T. W. He, J. J. Duan, Improved thermoelectric performance in Pr and Sr Co-doped $CaMnO_3$ materials, J. Alloy. Compd. 808 (2019) 151476.

[33] M. Mouyane, B. Itaalit, Flash Combustion Synthesis of electron doped-$CaMnO_3$ thermoelectric oxides, Powder Technol. 264 (2014) 71-77.

[34] Y. C. Zhou, C. L. Wang, W. B. Su, J. Liu, H. C. Wang, J. C. Li, Y. Li, J. Z. Zhai, Y. C. Zhang, L. M. Mei, Electrical properties of Dy^{3+}/Na^{+} Co-doped oxide thermoelectric $[Ca_{1-x}(Na_{1/2}Dy_{1/2})_x]MnO_3$ ceramics, J. Alloy. Compd. 680 (2016) 129-132.

[35] D. Flahaut, J. Allouche, A. Sotelo, Sh. Rasekh, M. A. Torres, M. A. Madre, J. C. Diez, Role of Ag in textured-annealed $Bi_2Ca_2Co_{1.7}O_x$ thermoelectric ceramic, Acta Mater. 102 (2016) 273-283.

[36] B. Zhang, A. Chang, Q. Zhao, H. Ye, Y. Wu, Synthesis and Thermoelectric Properties of Yb-doped $Ca_{0.9-x}Yb_xLa_{0.1}MnO_3$ Ceramics, J. Electron. Mater. 43 (2014) 4048-4055.

[37] H. Wang, C. Wang, Synthesis of Dy doped $Yb_{0.1}Ca_{0.9}MnO_3$ ceramics with a high relative density and their thermoelectric properties, Mater. Res. Bull. 47 (2012) 2252-2256.

[38] Y. Zhu, C. Wang, H. Wang, W. Su, J. Liu, J. Li, Influence of Dy/Bi dual doping on thermoelectric performance of $CaMnO_3$ ceramics, Mater. Chem. Phys. 144 (2014) 385-389.

[39] G. Xu, R. Funahashi, I. Matsubara, M. Shikano, Y. Zhou, High-temperature thermoelectric properties of the $Ca_{1-x}Bi_xMnO_3$ system, J. Mater. Res. 17 (2002) 1092-1095.

[40] R. Kabir, R. Tian, T. Zhang, R. Donelson, T. T. Tan, S. Li, Role of Bi doping in thermoelectric properties of $CaMnO_3$, J. Alloy. Compd. 628 (2015) 347-351.

[41] G. S. Nolas, G. Fowler, Assessing the role of filler atoms on the thermal conductivity of filled skutterudites, J. Appl. Phys. 100 (2006) 043705.

[42] P. Kayser, F. Serrano-Sanchez, O. J. Dura, F. Fauth, J. A. Alonso, Experimental corroboration of the thermoelectric performance of Bi_2PdO_4 oxide and Pb-doped derivatives, J. Mater. Chem. C 8 (2020) 5509-5516.

[43] T. Chen, J. Wang, X. Wang, H. Wang, W. Su, J. Zhai, F. Mehmood, M. Khan, C. Wang, Cross-scale porous structure design leads to optimized thermoelectric performance and high output power for $CaMnO_3$ ceramics and their uni-leg modules, Appl. Mater. Today 29 (2022) 101557.

[44] Y. Wang, Y. Sui, W. H. Su, High temperature thermoelectric characteristics of $Ca_{0.9}R_{0.1}MnO_3$ (R = La, Pr, …,Yb), J. Appl. Phys. 104 (2008) 093703.

[45] Y. Wang, Y. Sui, H. Fan, X. Wang, W. Su, X. Liu, High temperature thermoelectric response of electron-doped $CaMnO_3$, Chem. Mater. 21 (2009) 4653-4660.

[46] A. Bhaskar, C. Liu, J. Yuan, Thermoelectric and magnetic properties of $Ca_{0.98}Re_{0.02}MnO_{3-\delta}$ (Re=Sm, Gd and Dy), J. Electron. Mater. 41 (2012) 2338-2344.

Figure captions

Figure 1. SEM micrographs of milled $Ca_{1-x}(Y,La,Yb)_xMnO_3$ powders before cold uniaxial pressing, for x: a) 0.0; b) 0.01; c) 0.02; and d) 0.03.

Figure 2. (a) Powder XRD patterns of the $Ca_{1-3x}Y_xLa_xYb_xMnO_3$ samples for x = a) 0.0; b) 0.01; c) 0.02, and d) 0.03. Diffracted peaks are indexed considering the Pnam setting expected for the $CaMnO_3$ phase; (b) Enlarged observed (red) and calculated (black) XRD spectra considering $CaMnO_3$ (first line green index) and $CaMn_2O_4$ (second line green index) structures.

Figure 3. (a) Typical crystallite TEM micrograph recorded on $Ca_{0.91}Y_{0.03}La_{0.03}Yb_{0.03}MnO_3$ sample and corresponding elemental cation distribution; (b) Experimental HREM image collected on a part of a crystallite; (c) atomic STEM imaging; and (d) corresponding elemental cation profile.

Figure 4. Representative SEM micrographs obtained on the surface of $Ca_{1-3x}Y_xLa_xYb_xMnO_3$ samples for x = a) 0.0; b) 0.03.

Figure 5. Variation of electrical resistivity with temperature in $Ca_{1-3x}Y_xLa_xYb_xMnO_3$ samples, as a function of dopant content.

Figure 6. Temperature dependence of Seebeck coefficient in $Ca_{1-3x}Y_xLa_xYb_xMnO_3$ samples, as a function of dopant content.

Figure 7. Temperature dependence of the power factor in $Ca_{1-3x}Y_xLa_xYb_xMnO_3$ samples, as a function of dopant content.

Figure 8. Temperature dependence of the total thermal conductivity in $Ca_{1-3x}Y_xLa_xYb_xMnO_3$ samples, as a function of dopant content.

Figure 9. Temperature dependence of the lattice and electronic thermal conductivity in $Ca_{1-3x}Y_xLa_xYb_xMnO_3$ samples, as a function of dopant content.

Figure 10. Fitting of κ_{ph} thermal evolution using the Callaway's model for all samples.

Figure 11. Temperature dependence of ZT in $Ca_{1-3x}Y_xLa_xYb_xMnO_3$ samples, as a function of dopant content.

Table 1. Mean grain sizes, together with their standard error, determined in the different samples through the Z-potential technique.

Composition	Mean grain size (nm)	Error (nm)
$CaMnO_3$	578	35
$Ca_{0.97}Y_{0.01}La_{0.01}Yb_{0.01}MnO_3$	504	30
$Ca_{0.94}Y_{0.02}La_{0.02}Yb_{0.02}MnO_3$	412	37
$Ca_{0.91}Y_{0.03}La_{0.03}Yb_{0.03}MnO_3$	394	28

Table 2. Cell parameters evolution versus x in $Ca_{1-3x}Y_xLa_xYb_xMnO_3$ samples

Composition	a (Å)	b (Å)	c (Å)	$CaMn_2O_4$ phase content (vol.%)
x=0	5.2861(3)	7.4572(5)	5.2682(3)	1.97
x=0.01	5.2942(4)	7.4648(5)	5.2728(5)	3.47
x=0.02	5.3005(4)	7.4699(6)	5.2786(5)	2.56
x=0.03	5.3045(4)	7.4736(7)	5.2814(5)	1.35

Table 3. Mean grain sizes, together with their standard error, determined on sintered materials through the line-intercept method, and absolute density values, with their standard error determined by the Archimedes' method.

Composition $Ca_{1-3x}Y_xLa_xYb_xMnO_3$	**Mean grain size (μm)**	**Error (μm)**	**Density (g/cm^3)**	**Error (g/cm^3)**
x = 0	14.6	1.5	4.16	0.07
x = 0.01	8.8	0.3	4.27	0.06
x = 0.02	8.2	0.3	4.36	0.07
x = 0.03	7.5	0.3	4.44	0.05

Table 4. Point defect and phonon-phonon scattering parameters obtained from the fitting of κ_{ph} thermal evolution using the Callaway's model for all samples.

Composition	A (point defects)	B (phonon-phonon)
$CaMnO_3$	$6.61\ 10^{-19}$	$5.07\ 10^{-19}$
$Ca_{0.97}Y_{0.01}La_{0.01}Yb_{0.01}MnO_3$	$1.37\ 10^{-18}$	$1.01\ 10^{-20}$
$Ca_{0.94}Y_{0.02}La_{0.02}Yb_{0.02}MnO_3$	$1.67\ 10^{-18}$	$2.27\ 10^{-18}$
$Ca_{0.91}Y_{0.03}La_{0.03}Yb_{0.03}MnO_3$	$2.08\ 10^{-18}$	$7.49\ 10^{-18}$

Figure 1

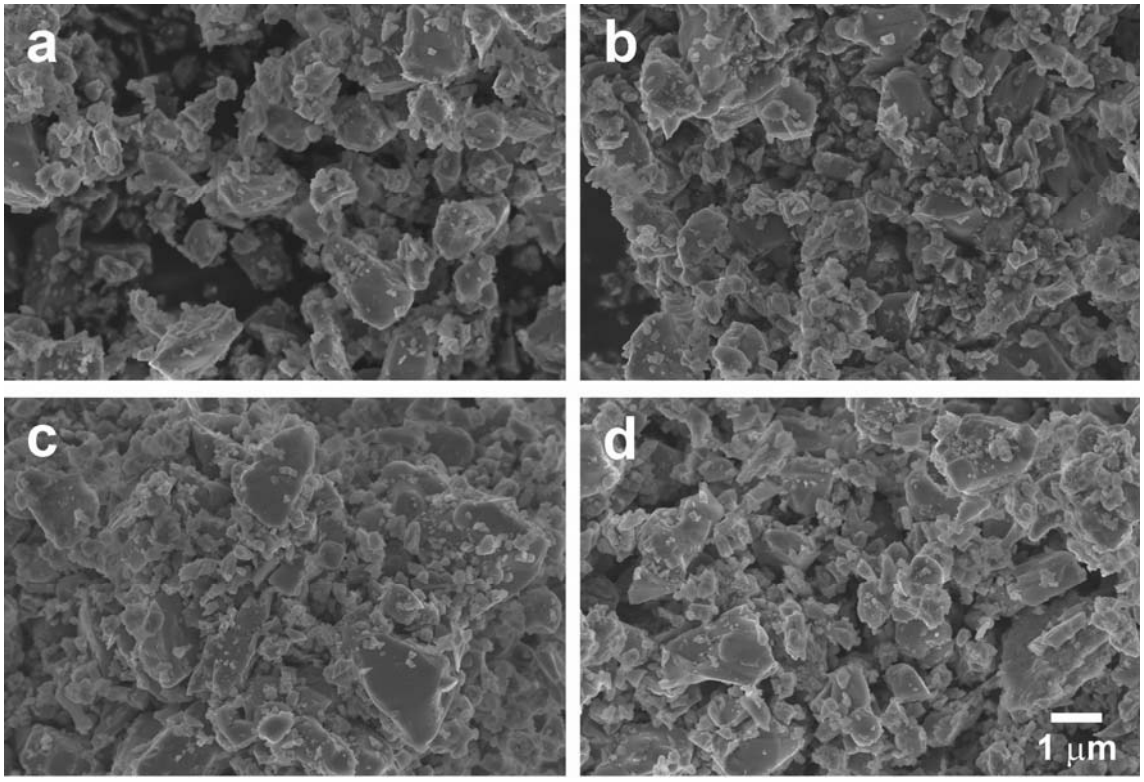

Figure 2

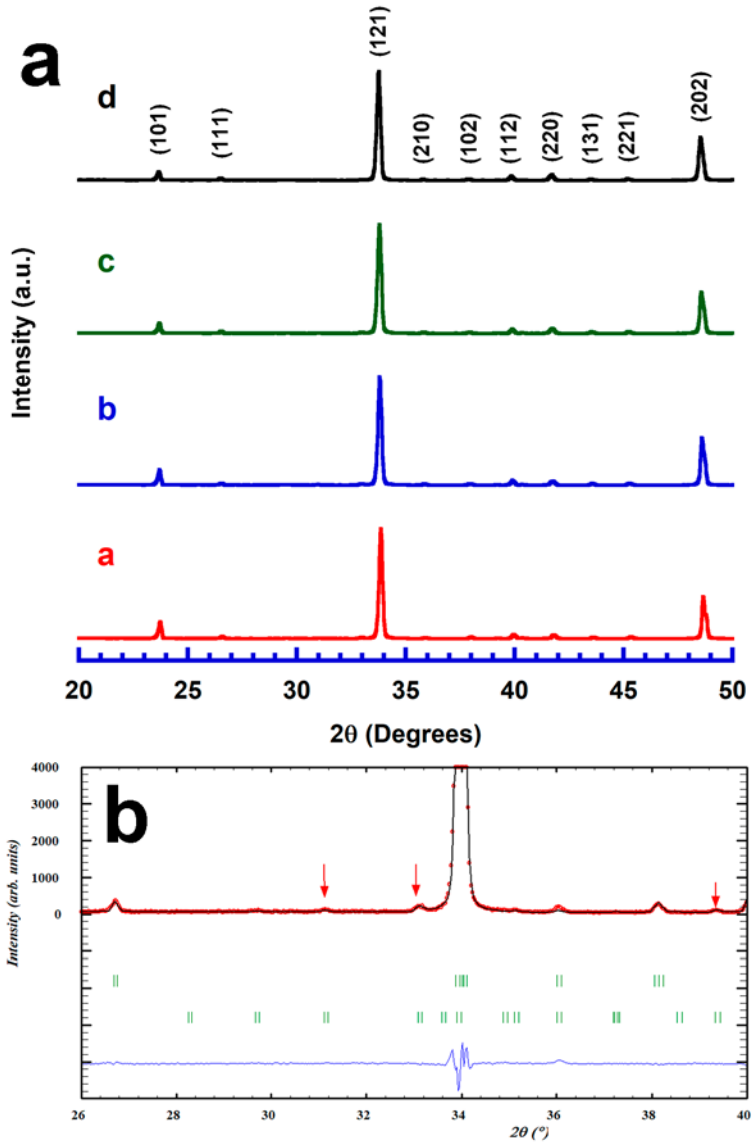
a
d
c
b
a
(101)
(111)
(121)
(210)
(102)
(112)
(220)
(131)
(221)
(202)
Intensity (a.u.)
20
25
30
35
40
45
50
2θ (Degrees)
b
Intensity (arb. units)
4000
3000
2000
1000
0
26
28
30
32
34
36
38
40
2θ (°)

Figure 3

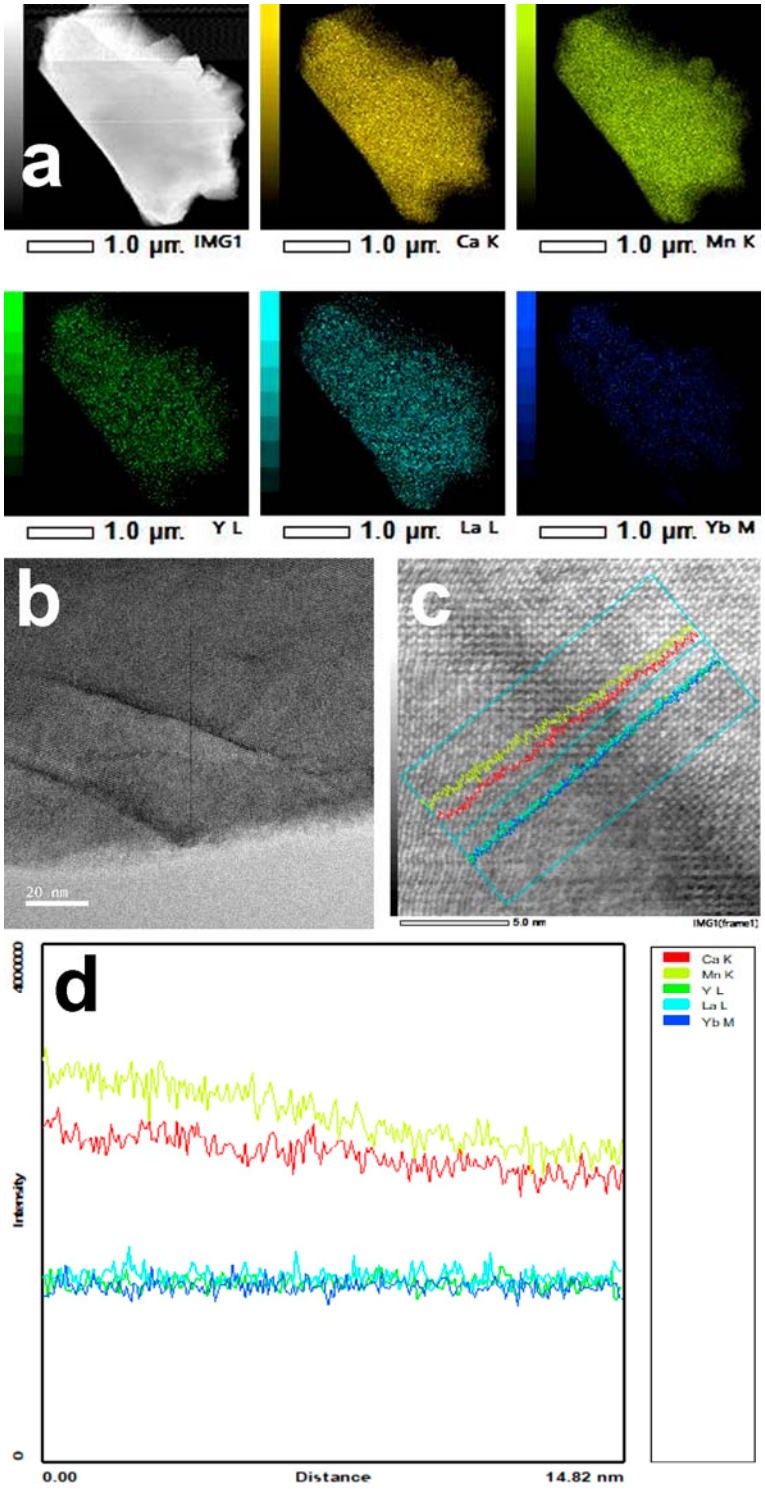
a
1.0 µm. IMG1
1.0 µm. Ca K
1.0 µm. Mn K
1.0 µm. Y L
1.0 µm. La L
1.0 µm. Yb M
b
20 nm
c
5.0 nm
IMG1[frame1]
d
Ca K
Mn K
Y L
La L
Yb M
Intensity
0
0.00
Distance
14.82 nm

Figure 4

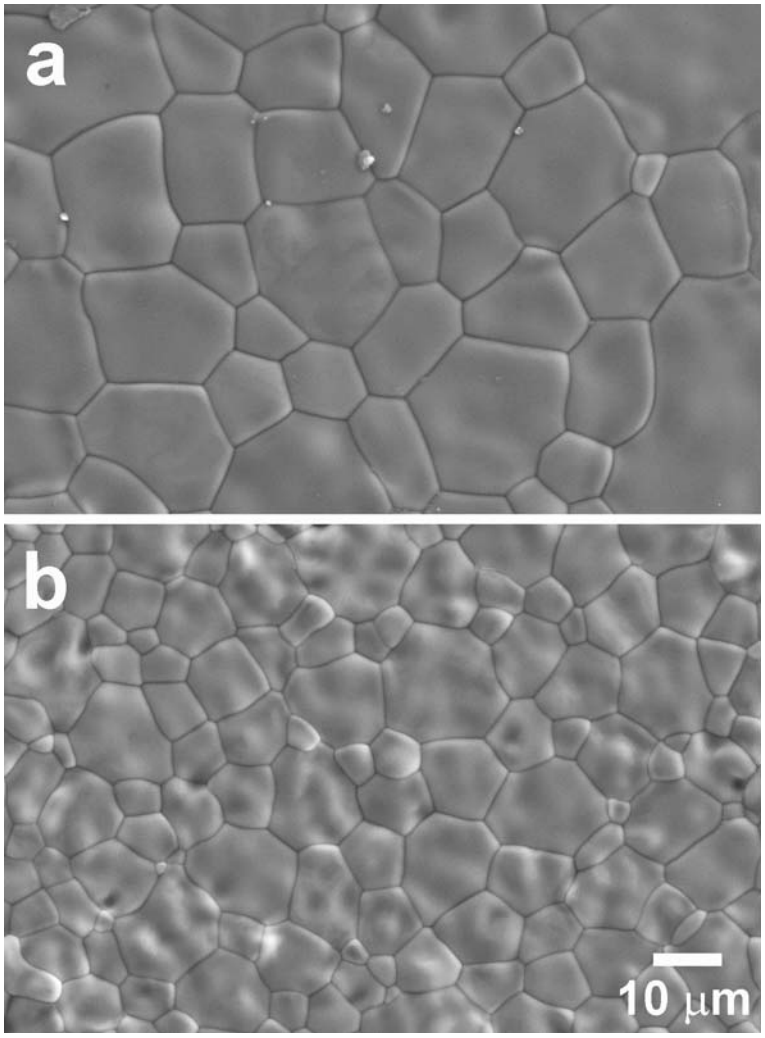

Figure 5

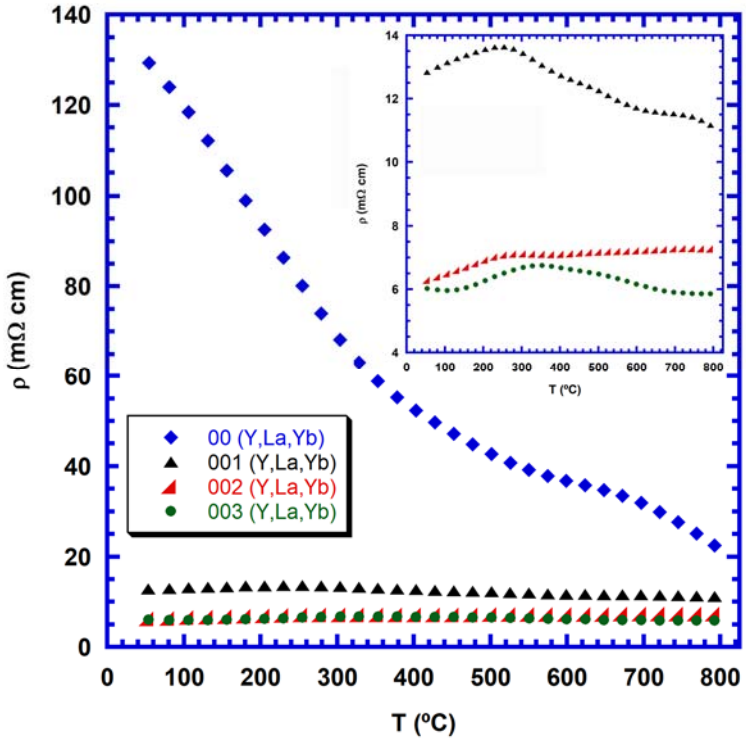

Figure 6

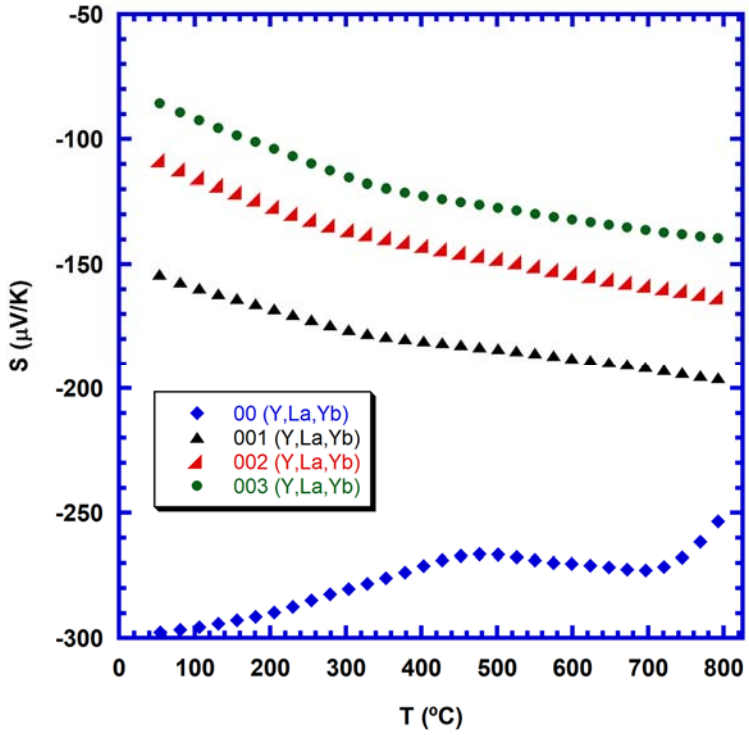
-50
-100
-150
-200
-250
-300
S (μV/K)
0
100
200
300
400
500
600
700
800
T (°C)
00 (Y,La,Yb)
001 (Y,La,Yb)
002 (Y,La,Yb)
003 (Y,La,Yb)

Figure 7

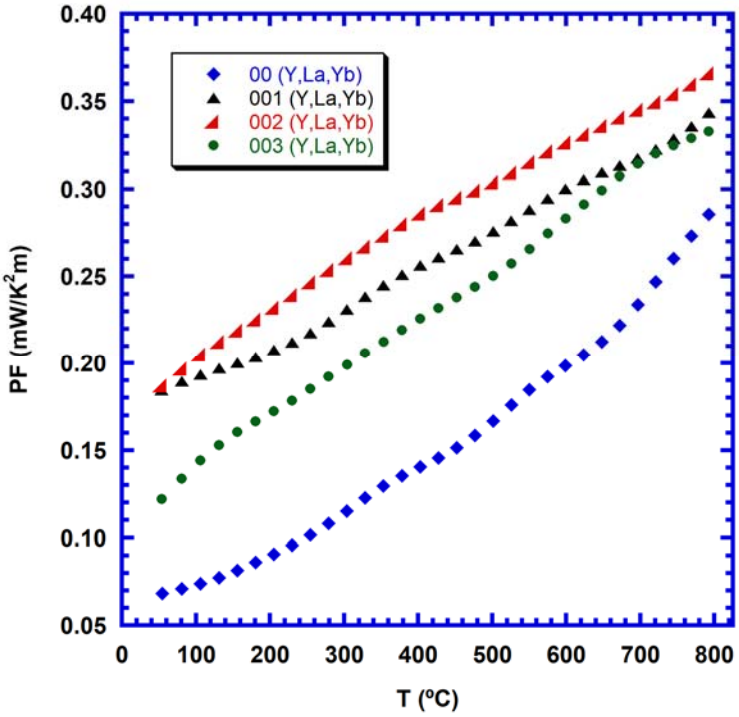
00 (Y,La,Yb)
001 (Y,La,Yb)
002 (Y,La,Yb)
003 (Y,La,Yb)
PF (mW/K²m)
T (ºC)
0.40
0.35
0.30
0.25
0.20
0.15
0.10
0.05
0
100
200
300
400
500
600
700
800

Figure 8

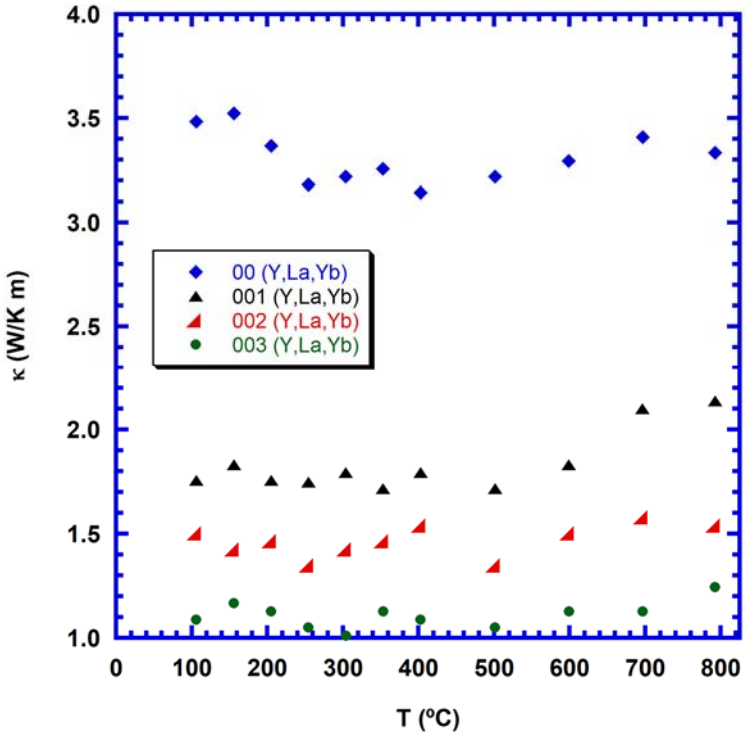
4.0
3.5
3.0
2.5
2.0
1.5
1.0
κ (W/K m)
0
100
200
300
400
500
600
700
800
T (°C)
00 (Y,La,Yb)
001 (Y,La,Yb)
002 (Y,La,Yb)
003 (Y,La,Yb)

Figure 9

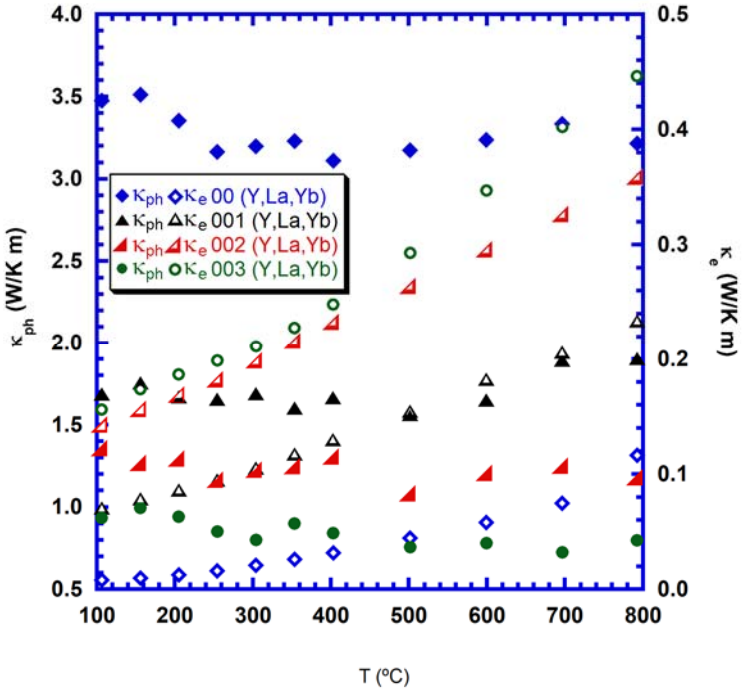
4.0
3.5
3.0
2.5
2.0
1.5
1.0
0.5
κph (W/K m)
0.5
0.4
0.3
0.2
0.1
0.0
κe (W/K m)
100
200
300
400
500
600
700
800
T (ºC)
κph κe 00 (Y,La,Yb)
κph κe 001 (Y,La,Yb)
κph κe 002 (Y,La,Yb)
κph κe 003 (Y,La,Yb)

Figure 10

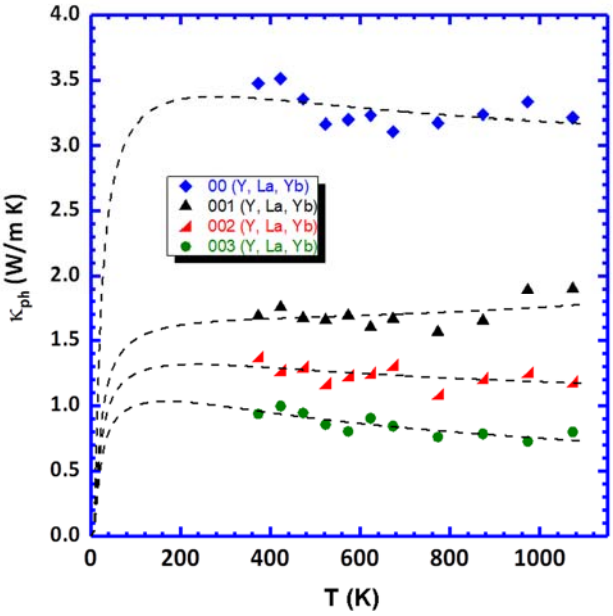
4.0
3.5
3.0
2.5
2.0
1.5
1.0
0.5
0.0
0
200
400
600
800
1000
T (K)
κph (W/m K)
00 (Y, La, Yb)
001 (Y, La, Yb)
002 (Y, La, Yb)
003 (Y, La, Yb)

Figure 11

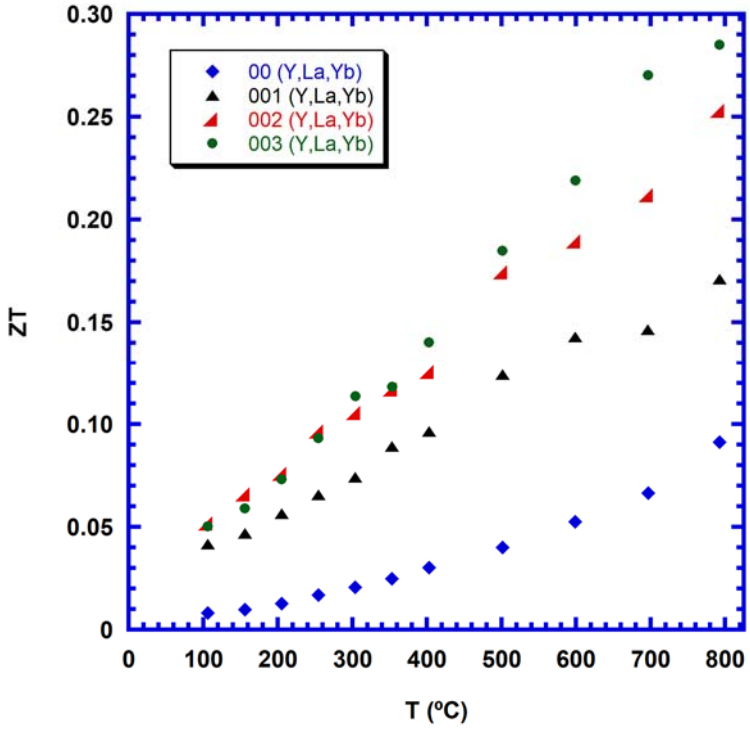
00 (Y,La,Yb)
001 (Y,La,Yb)
002 (Y,La,Yb)
003 (Y,La,Yb)
ZT
T (°C)
0.30
0.25
0.20
0.15
0.10
0.05
0
0
100
200
300
400
500
600
700
800